Journal of Catalysis 332 (2015) 201–211

Contents lists available at ScienceDirect

Journal of Catalysis

journal homepage: www.elsevier.com/locate/jcat

# Unprecedented propane–SCR-$NO_x$ activity over template-free synthesized Al-rich Co-BEA* zeolite

Petr Sazama *, Lukasz Mokrzycki, Blanka Wichterlova, Alena Vondrova, Radim Pilar, Jiri Dedecek, Stepan Sklenak, Edyta Tabor

J. Heyrovský Institute of Physical Chemistry, Academy of Sciences of the Czech Republic, CZ-182 23 Prague 8, Czech Republic

ARTICLE INFO

*Article history:*
Received 24 June 2015
Revised 23 September 2015
Accepted 3 October 2015
Available online 12 November 2015

*Keywords:*
Beta zeolite
Al-rich BEA*
OSDA-free synthesis
Cobalt
Selective catalytic reduction of nitrogen oxides
SCR-$NO_x$
Propane
Hydrocarbons
FTIR
UV–Vis spectroscopy

ABSTRACT

An Al-rich Co-BEA* zeolite (Si/Al 4.2, Co/Al 0.5) was prepared by organotemplate-free hydrothermal synthesis and $[Co(II)(H_2O)_6]^{2+}$ ion exchange. The structure of the Co species and their activity in $C_3H_8$–SCR-$NO_x$ were compared to that of Si-rich Co-BEA* (Si/Al 11.3). The high population of AlSiAl sequences in Al-rich BEA* with $AlO_4^-$ facing different channels, contrary to their absence in Si-rich BEA*, results in dehydrated Co-BEA* in easily reducible counter-ion $[Co(III)O]^+$ species attached to one $AlO_4^-$. The high concentration and density of these Co-oxo species in Al-rich Co-BEA* facilitates extraordinarily high SCR-$NO_x$ rate even under water vapor up to 10 vol.%, twelve-times outperforming Si-rich Co-BEA*. The five-to-six times increased TOF and easier reducibility suggest a synergetic redox effect of water-resistant Co-oxo species. The Al-rich Co-BEA* provides the highest reaction rate at conditions of wet $NO_x$ streams, exceeding that previously reported for metal ion/oxo zeolite catalysts, with a high selectivity to molecular nitrogen and efficient utilization of propane.

## 1. Introduction

Development of a functional catalyst for selective catalytic reduction of nitrogen oxides by hydrocarbons, particularly propane, methane or long-chain paraffins (SCR-$NO_x$) under real $NO_x$ streams containing low concentrations of $NO/NO_2$ (~1000 ppm) in the presence of high concentration of water vapor (1–10%) remains a great challenge for heterogeneous catalysis [1–5]. Cobalt counter-ion species in conventional (Si-rich, Si/Al > 12) zeolites of BEA* and MFI topology have so far exhibited the highest SCR-$NO_x$ activity and selectivity in reduction of $NO_x$ to nitrogen by propane in a broad temperature range among all the types of investigated catalysts [2,6–8]. Besides stabilization of various types of counter-ion Co species, the advantage of these crystalline matrices lies in their three-dimensional channel structures with 10-member ring (10MR) openings for MFI and particularly with 12MR openings for BEA* topology offering fast intra-crystalline diffusion of reactants and products through zeolite pores [7].

The concentration, structure and location of incorporated Co species represent key parameters governing the SCR activity and selectivity for nitrogen [9–18], which are inevitably controlled by the overall and local negative charge of the zeolite framework [19,20]. For the Si-rich Co-beta and Co-ZSM-5 zeolites, it has been shown that the single exchanged Co(II) ions coordinated exclusively with the oxygen atoms of the framework rings containing Al pairs (AlSiSiAl sequences) and forming cationic sites are active in propane–SCR-$NO_x$ [21,22] only in the absence of water vapor or at temperatures when water adsorption does not take place on these electron-acceptor Co sites. Much higher activity, which is moreover preserved in wet gas streams, was found for counter-ion Co-oxo species adjacent to isolated framework Al atoms and populated predominantly at higher Co loadings in ZSM-5 and beta zeolites [21,22].

To reach high concentration of incorporated counter-ion Co species, moreover, of appropriate structure and redox properties relevant for the SCR-$NO_x$ reaction, a high concentration of Al atoms in the framework and their optimal mutual arrangement are necessary [22]. The concentration of the active Co-oxo species could be increased at the expense of less active bare Co(II) species by

---

* Corresponding author.
*E-mail address:* petr.sazama@jh-inst.cas.cz (P. Sazama).

http://dx.doi.org/10.1016/j.jcat.2015.10.007
0021-9517/© 2015 Elsevier Inc. All rights reserved.

optimizing the distribution of Al atoms in the framework of the parent zeolites [21].

The recently discovered new procedure for the hydrothermal synthesis of the Al-rich beta zeolite with a high concentration of Al in the framework has opened the way for preparation of Co zeolite-based catalysts with a high concentration of Co species. Borade and Clearfield [23,24] developed a new synthesis route for high substitution of Al in the tetrahedrally coordinated $SiO_4$ framework of the beta zeolite (Si/Al 4.5) from a dense system containing a minimum of template. Later studies [25–37] led to the synthesis of Al-rich beta zeolites of Si/Al $\geqslant 4$ employing seeding of Si-rich BEA* crystals and in the complete absence of an organic structure-directing agent like tetraethyl ammonium hydroxide (TEAOH). The first results showing the prospect for Al-rich beta zeolites as a base for redox catalysts have been reported for Fe [37,38], Cu [39], and Pt [40] catalysts. Al-rich Fe-BEA* reached the highest activity among Fe-zeolite catalysts in $NH_3$–SCR-$NO_x$, and substantially enhanced the reaction rate in $N_2O$ decomposition [37] and capture of NO at low concentrations [41].

In this study we show the superior activity of the Al-rich Co-beta zeolite in propane–SCR-$NO_x$, even in the presence of water vapor, remarkably outperforming that of the so-far most active Si-rich Co-BEA* and Co-MFI catalysts. Detail analysis of the arrangement of Al atoms in the framework of Al-rich beta zeolites described in an preceded paper [42] enabled investigation of the structure, location and activity of Co species in propane–SCR-$NO_x$ with regard to the arrangement of framework Al atoms and to compare it to those of Si-rich Co-BEA*.

## 2. Experimental

### 2.1. Preparation of Co-zeolites

Al-rich BEA* was hydrothermally synthesized using a template-free procedure with seeding of calcined beta crystals (TBZ 212, Tricat) and an aluminosilicate mixture with a molar ratio of $Al_2O_3$/$SiO_2$/NaOH/$H_2O$ 1.00:31.7:20.7:1110.5 originating from $NaAlO_2$ (Sigma Aldrich, 13404, Lot # SZBA2440), fumed silica (Aerosil) and NaOH. The synthesis gel was prepared by mixing 8.0 g of fumed silica, 3.475 g of NaOH, 0.775 g of $NaAlO_2$, 82.00 g $H_2O$ and 0.400 g of zeolite seeds. Hydrothermal synthesis was performed in 200 ml autoclaves without agitation at a temperature of 120 °C under autogeneous pressure for 120 h. The obtained zeolite with a molar Si/Al ratio 4.2 was denoted as BEA/4.2. The beta zeolite with Si/Al 11.3 (CP814B-25, Lot. No. 814B-25-1597-77, denoted as BEA/11), was kindly supplied by Zeolyst International as a material widely used for preparation of zeolite catalysts. The template was removed by careful zeolite heating in an ammonia stream followed by calcination up to 550 °C according to the procedure described in Ref. [37]. ZSM-5 with Si/Al (15.3) provided by the Research Institute of Petroleum and Hydrocarbon Gases (Slovnaft, Slovakia) was denoted as ZSM-5/15 (see the Supplementary Materials). The composition of BEA* zeolites is given in Table 1. Detailed structural analysis of the BEA/11 and ZSM-5/15 parent zeolites has been reported elsewhere [37,43].

All the zeolites were ion-exchanged three times with 0.5 M $NH_4NO_3$ to obtain the $NH_4^+$-form. Co-BEA/4.2, Co-BEA/11 and Co-ZSM-5/15 were prepared by threefold ion-exchange at RT (24 h) of the respective zeolites in their $NH_4^+$ forms with 0.05 M aqueous $Co(NO_3)_2$ solution (100 ml $g^{-1}$) followed by washing with demineralized water and drying in the open air. The chemical composition of Co-BEA* zeolites is given in Table 2.

### 2.2. Structural analysis

X-ray diffractograms were recorded using a Bruker D8 instrument (Bruker AXS), the $N_2$ sorption at 77 K and scanning electron micrographs were obtained by an ASAP2020 Micromeritics apparatus and Jeol JSM-03 microscope, respectively. A Bruker Avance 500 MHz (11.7 T) Wide Bore spectrometer was used to measure the $^{27}$Al and $^{29}$Si MAS NMR spectra of the fully hydrated parent zeolites. $ZrO_2$ rotors with a rotation speed of 12 kHz and high-power decoupling pulse sequences with a $\pi/12\pi$ (0.7 μs) excitation pulse and 1 s relaxation delay were used. Chemical shifts were referenced to an aqueous solution of $Al(NO_3)_3$. $^{29}$Si MAS NMR single pulse spectra were measured at a rotation speed of 5 kHz with a $\pi/6$ (1.7 μs) excitation pulse and relaxation delay of 30 s. The framework $Si/Al_{FR}$ ratio was estimated according to the equation

$$Si/Al_{FR} = I/(0.25I_1 + 0.5I_2) \quad (1)$$

where $I_1$ denotes the intensity of the NMR lines corresponding to the Si(3Si,1Al) atoms, $I_2$ to Si(2Si,2Al) atoms and I denotes the total $^{29}$Si intensity; for details see Ref. [44].

The FTIR spectra of H- and Co-BEA* zeolites were measured, after evacuation at 450 °C for 3 h, in the region of the OH mode and after adsorption of $d_3$-acetonitrile (13 mbar) at RT followed by evacuation at RT for 20 min (for H-BEA*) and after evacuation at 200 °C for 30 min (for Co-BEA*). The latter procedure suppressed adsorption of $CD_3CN$ on Brønsted sites (2293 $cm^{-1}$) and enabled quantitative analysis of the intensity of the C≡N vibrations connected with bare Co(II) ions (2308 $cm^{-1}$) by using extinction coefficient $\varepsilon = 7.12$ cm $\mu mol^{-1}$ [22]. A Nicolet 6700 FTIR spectrometer operating at a resolution of 1 $cm^{-1}$ and collecting 256 scans for a single spectrum was employed. Temperature-programmed reduction of Co-zeolites by hydrogen ($H_2$-TPR) was monitored by an Altamira AMI-200 instrument on samples pre-treated in a stream of air at 450 °C for 1 h and then cooled to 35 °C. Reduction of samples by hydrogen was carried out at a heating rate of 10 °C $min^{-1}$ from 35 to 1000 °C using an $H_2$/Ar stream (9.44 vol.% $H_2$) with a flow rate of 30 ml $min^{-1}$. The UV–Vis–NIR reflectance spectra of Co-zeolites evacuated at 500 °C were recorded on a Perkin-Elmer Lambda 950 UV–Vis–NIR spectrometer equipped with an integrating sphere covered by Spectralon®, which also served as a reference. The reflectance was calculated using the Schuster–Kubelka–Munk function $F(R_\infty) = (1 - R_\infty)^2/2R_\infty$, where $R_\infty$ is the diffuse reflectance from a semi-infinite layer. $F(R_\infty)$ is proportional to the absorption coefficient for $F(R_\infty) < 0.5$.

The concentration of bare Co(II) ions in dehydrated Co-BEA* was estimated from the intensity of the characteristic IR band at 2308 $cm^{-1}$ of adsorbed $d_3$-acetonitrile on Co(II)-$\beta$ ions (the only one of Co(II) ions accessible to $CD_3CN$ molecules in both the

**Table 1**
Characteristics of parent zeolites.

| Sample | Si/Al[a] | $Si/Al_{FR}$[b] | $c_{Al}$[a] (mol $g^{-1}$) | $c_B$[c] (mol $g^{-1}$) | $c_L$[c] (mol $g^{-1}$) | Crystal size (μm) | S ($m^2$ $g^{-1}$) |
|---|---|---|---|---|---|---|---|
| BEA/4.2 | 4.2 | 4.7 | 3.0 | 1.80 | 0.22 | ~0.4 | 510 |
| BEA/11 | 11.3 | 11.5 | 1.4 | 0.63 | 0.32 | ~0.05 | 617 |

[a] From chemical analysis of Na-BEA*.
[b] From $^{29}$Si MAS NMR spectra of Na-BEA*.
[c] Concentration of Brønsted and Al-Lewis sites from FTIR spectra of adsorbed $d_3$-acetonitrile.

**Table 2**
Composition and concentration of bare Co(II) ions, Co-oxo species and Al-Lewis acid sites in Co-BEA*.

| Sample | Co/Al[a] | $c_{Co}$[a] | | $c_{Co(II)\text{-}\beta}$[b] | $c_{Co(II)}$[c] | $c_L$[b] | $c_{Co\text{-}oxo}$[d] | $H_2$/Co | $c_{Co\text{-}oxo}$[e] |
|---|---|---|---|---|---|---|---|---|---|
| | | wt.% | mmol $g^{-1}$ | mmol $g^{-1}$ | | | | | mmol $g^{-1}$ |
| Co-BEA/4.2 | 0.54 | 8.7 | 1.47 | 0.55 | 0.62 | 0.04 | 0.85 | 1.37 | 0.91 |
| Co-BEA/11 | 0.53 | 4.1 | 0.69 | 0.20 | 0.30 | 0.03 | 0.39 | 0.57 | 0.38 |

[a] From chemical analysis of Co-BEA*.

[b] Concentration of Co(II)-$\beta$ ions and Al-Lewis sites from FTIR spectra of adsorbed $d_3$-acetonitrile.

[c] Total concentration of bare Co(II) ions estimated from the relative concentrations of Co(II)-$\alpha$, Co(II)-$\beta$ and Co(II)-$\gamma$ ions from Vis spectra.

[d] Concentration of Co-oxo species calculated as a difference between $c_{Co}$ and $c_{Co(II)}$.

[e] Concentration of Co-oxo species calculated from $H_2$-TPR.

Al-rich and Si-rich Co-BEA*) and relative intensities of the Vis absorptions of Co(II) ions of the $\alpha$-, $\beta$-, $\gamma$- and $\varepsilon$-types as elaborated in detail in Ref. [42]. The concentration of Co-oxo species was calculated as a difference of total Co content and sum of concentrations of Co(II)-$\alpha$, Co(II)-$\beta$ and Co(II)-$\gamma$ ions coordinated with rings of cationic sites containing AlSiSiAl sequences. The concentration of Co(II)-$\varepsilon$ ions was low, <5% of total Co.

### 2.3. Selective catalytic reduction of $NO_x$ by propane

The reaction of $C_3H_8$–SCR-$NO_x$ was performed using a quartz tubular down-flow reactor with 100 mg of a catalyst in the form of 0.3–0.5 mm grains. A typical reactant mixture consisting of 1000 ppm NO, 1000 $C_3H_8$, 2.5% $O_2$ and 1–10% $H_2O$ in He as a balance was kept at a total flow rate of 300 ml $min^{-1}$ corresponding to GHSV 90000 $h^{-1}$. The concentrations of $NO_x$ (NO, $NO_2$) and $N_2O$ in the inlet and outlet of the reactor were continuously monitored by an NO/$NO_x$ chemiluminescence analyzer (API MLU 200AH) and IR analyser (ABB Advance Optima Uras 14), respectively. An on-line-connected Hewlett Packard 6090 gas chromatograph was used for analysis of the concentrations of $C_1$–$C_4$ hydrocarbons, $O_2$, $N_2$, $N_2O$, CO, and $CO_2$. Two gaseous samples were simultaneously injected through 10-port valves into two branches of the gas chromatograph equipped with a thermal conductivity detector (TCD) for analysis of $O_2$, $N_2$, $N_2O$, CO, and $CO_2$, and a flame ionization detector (FID) for analysis of $C_1$–$C_4$ hydrocarbons (for more details see Ref. [45]). The concentrations of the reactants and products were read stepwise under steady-state reaction conditions at temperatures from 450 to 250 °C. $NO_x$ conversion is defined as the reduction of NO and $NO_2$ to $N_2$ and $N_2O$. The catalytic tests were repeated twice, and the reproducibility in $NO_x$ conversion was ±2%. Conversion of $C_3H_8$ was calculated from the results of GC-FID analysis. $CO_2$ and CO were the major products and small quantities of methane, ethane, ethene, traces of butanes, butenes were found in the reactor outlet. As the yields of these products were well below 1%, they are not reported in the results. The influence of external mass and heat transfer on the SCR reaction was excluded by experiments with variations in the catalyst weights and flow rates at constant GHSV, where conversions of $NO_x$ and $C_3H_8$ did not change within ±2%. The crystal sizes of parent zeolites < 1 μm guaranteed the absence of intra-crystalline diffusion constraints, as shown in preceding studies [46,47]. The rates of the $NO_x$ reaction ($r_{SCR}$) per gram of catalyst (mol $g^{-1}$ $s^{-1}$) were calculated using the assumption of pseudo-first-order kinetics with equation written as $r = F/W * (-\ln(1-x))$, where $F$ is the flow rate of the feed (mol of NO per s) and $W$ is the weight of the catalyst (g). Only the $C_3H_8$ conversion values <30% were considered. Changes in the oxygen and water concentrations resulting from the reaction do not affect the reaction rate, as they are present in high excess. The turn-over-frequencies (TOF) were expressed in terms per total Co ($mol_{NO}\ mol_{Co}^{-1}\ s^{-1}$) and per Co-oxo ($mol_{NO}\ mol_{Co\text{-}oxo}^{-1}\ s^{-1}$). The apparent activation energies and pre-exponential factors were estimated from the Arrhenius plots.

## 3. Results and discussion

### 3.1. Structure of BEA* zeolites

The organotemplate-free synthesis using crystal seeding provided Al-rich BEA* zeolite with a Si/Al molar ratio of 4.2. X-ray diffractograms (Fig. 1A) showed sharp and intensive reflections characteristic of a well-developed crystalline structure of BEA* topology formed by intergrowth of polymorphs A and B [48]. All reflection lines of BEA/4.2 were shifted by 0.3 to lower 2$\theta$ values compared to BEA/11, indicating an increase in the unit cell size due to the increased concentration of longer Al—O compared to Si—O bonds [49]. Nitrogen adsorption/desorption isotherms for BEA/4.2 resembled a sharp adsorption knee at very low pressure followed by a plateau without hysteresis characteristic of a purely microporous structure with micropore volume of 0.24 $cm^3\ g^{-1}$ (Fig. 1B). BEA/11 exhibited nitrogen adsorption at low pressures followed by its increase at higher relative pressures characteristic of small agglomerated crystallites with high external surface area. These sorption characteristics are consistent with a crystal size of ~0.4 and 0.05 μm for BEA/4.2 and BEA/11, respectively, estimated from the SEM images (Table 1).

The $^{27}$Al MAS NMR spectra of both Na-BEA* in the fully hydrated state showed resonances with the observed shift around 55 ppm corresponding to the tetrahedrally coordinated Al atoms in the framework (Fig. 1C). Resonances around 0 ppm and between 30 and 45 ppm reflecting extra-framework octahedral Al atoms and penta-coordinated or perturbed tetrahedral Al atoms [50,51], respectively, were not observed. The framework Al content (Si/$Al_{FR}$) calculated from the intensities of the characteristic resonances of $^{29}$Si MAS NMR spectra corresponding to the Si(4Si), Si(3Si,1Al) and Si(2Si,2Al) atoms for BEA/4.2 and the absence of Si(2Si,2Al) atoms in BEA/11 (Fig. 1D) were comparable with those obtained from chemical analysis (Table 1). Thus the synthesized BEA/4.2 zeolite exhibits well-developed microporosity within small crystallites and contains only tetrahedrally coordinated Al in the framework without the presence of perturbed or extra-framework Al atoms. The estimated limits of the concentrations of Al atoms in AlSiAl sequences for the possible Al arrangements in the framework for BEA/4.2, i.e. infinite $(AlSi)_n$ sequence or AlSiAl sequences forming rings, and isolated AlSiAl sequences (calculated according to Eqs. (6)–(9) given in Ref. [42]) ranged from 75% to 100% of total Al. On contrary to BEA/4.2, the Si-rich BEA/11 sample did not contain AlSiAl sequences.

### 3.2. Structure of Co species in Co-BEA* zeolites

#### 3.2.1. FTIR spectra of OH groups and adsorbed $d_3$-acetonitrile on H- and Co-BEA*

Fig. 2A shows FTIR spectra in the region of $\nu$(O—H) vibration mode of H-BEA* and after ion exchange of $NH_4$-BEA* by Co(II) ions. The spectra of H-BEA/4.2 and H-BEA/11 exhibit typical OH vibrations in beta zeolites with the sharp intensive bands of

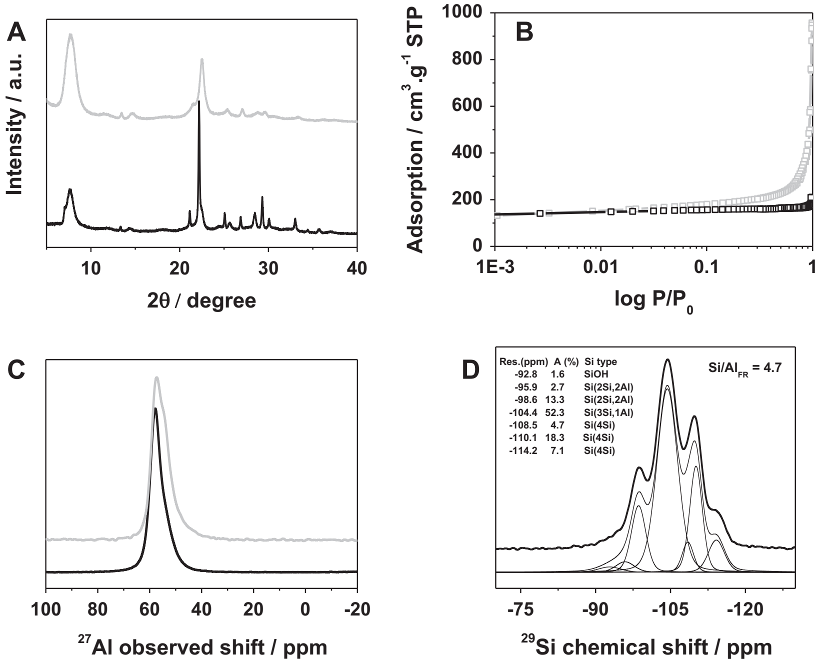

**Fig. 1.** Characteristics of BEA/4.2 (black) and BEA/11 (gray) zeolites. (A) X-ray diffraction patterns, (B) $N_2$-sorption isotherms at 77 K, (C) $^{27}$Al MAS NMR and (D) $^{29}$Si MAS NMR spectra.

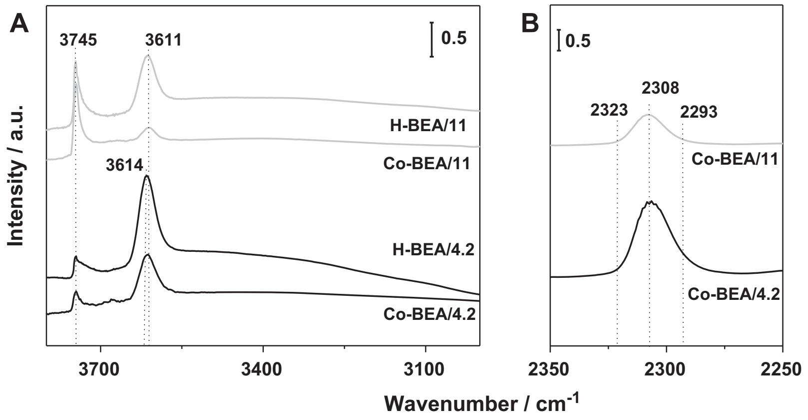

**Fig. 2.** FTIR spectra of H- and CoH-BEA* zeolites. (A) The region of $\nu$(O—H) vibrations after evacuation at 450 °C for 3 h and (B) $\nu$(C≡N) vibrations after adsorption of $d_3$-acetonitrile (13 mbar) at RT and evacuation at 200 °C for 30 min. C≡N vibrations at 2308 and 2323 $cm^{-1}$ on Co(II)-β ions and Al-Lewis sites, respectively.

non-interacting bridging hydroxyls (3614 and 3611 $cm^{-1}$, respectively) and the broad band ranging from 3620 to 3200 $cm^{-1}$ of mutually interacting SiOHAl groups. A higher intensity of the band of terminal SiOH groups (3745 $cm^{-1}$) for H-BEA/11 is due to small crystallites and high external surface area (cf. Table 1). The absence of vibrations at about 3650 $cm^{-1}$ and 3782 $cm^{-1}$ indicated the absence of the Al—OH groups of perturbed and extra-framework Al atoms [52]. A similar relative content of non-interacting and interacting SiOHAl in H- and Co-BEA* zeolites indicates replacement of both types of these groups by Co(II) ions. The Co ion-exchange capacity of $NH_4$-BEA* zeolites (Co/Al 0.54 and 0.53 for Co-BEA/4.2 and Co-BEA/11, respectively) shows that one $[Co(II)(H_2O)_6]^{2+}$ complex was exchanged for approximately two $AlO_4^-$. The occurrence of SiOHAl groups in the dehydrated Co-BEA* is in accordance with the binding of extra-framework oxygen atom by some Co ions adjacent to one $AlO_4^-$ as formally "monovalent" Co-oxo species, as discussed further.

Adsorption of $CD_3CN$ at RT on Co-BEA* resulted in the bands at 2323, 2308 and 2293 $cm^{-1}$ (not shown) of C≡N groups interacting with Al-Lewis sites, bare Co(II)-$\beta$ ions and Brønsted sites [53], respectively. Evacuation of Co-BEA* with adsorbed $CD_3CN$ at 200 °C for 20 min (Fig. 2B) considerably decreased the intensity at 2293 $cm^{-1}$, but quantitatively preserved that at 2308 $cm^{-1}$ of C≡N on bare Co(II)-$\beta$ ions and Al-Lewis sites. The 2.1 times higher concentration of bare Co(II)-$\beta$ ions for Co-BEA/4.2 compared to Co-BEA/11, determined from the intensity of the band at 2308 $cm^{-1}$, corresponds to the increase in the total Co content and roughly to Al content in the framework of Co-BEA/4.2 (see Table 2). The bare Co(II)-$\alpha$ and Co(II)-$\gamma$ ions are not accessible to $CD_3CN$ molecules [42]. The Co-oxo species prevailing in both Co-BEA* zeolites (see below) do not adsorb $CD_3CN$, in contrast to bare Co(II)-$\beta$ ions, as their coordination sphere is completed by an extra-framework oxygen atom (for details see Refs. [42,53]).

### *3.2.2. UV–Vis–NIR spectra of Co-BEA**

The UV–Vis–NIR spectra of the dehydrated Co-BEA/4.2 and Co-BEA/11 (Fig. 3) exhibited broad absorption of a complex shape in the region of d–d transitions at 13000–27000 $cm^{-1}$ of high-spin

Co(II) ion complexes containing exclusively framework oxygen ligands (bare Co(II) ions), and very low intensity of the ligand to metal O → Co(II) charge-transfer (LMCT) complexes of the $\mu$-oxo dinuclear Co species at 28 000–35 000 cm$^{-1}$ [53]. As the extinction coefficients of the LMTC transitions are ca 50× higher compared to those of the d–d transitions [53], the low intensity LMCT transitions of these bridged dinuclear Co complexes reflect their negligible concentration. The strong absorption increasing above 40 000 cm$^{-1}$ corresponds to LMCT transitions from the framework oxygen atoms to bare Co(II) ions in the cationic sites and transitions from extra-framework oxygen(s) to Co ions in Co-oxo species reaching frequencies well-above 50 000 cm$^{-1}$ [42], i.e. in a region unaccessible using the standard UV–Vis spectroscopy. While the quantitative analysis of these Co-oxo species from the UV spectra was therefore not possible, the clear presence of the latter LMCT in the UV range of the spectrum for Co-BEA* samples with the ion-exchange level of Co/Al ~ 0.5 could be related to the counter-ion Co-oxo species, and it is supported by the $H_2$-TPR experiment given in Fig. 5.

The detail analysis of the d–d transitions of bare Co(II) ions in Al-rich Co-BEA* zeolites (Si/Al 4.5 and 5.1) reported in the preceding paper [42], and based on the Vis spectral analysis of the coordination of Co(II) ions with different framework rings in Si-rich Co-BEA/11 and other pentasil ring (MFI, FER, MOR) zeolites, led to the conclusion that the bands at 14 850 cm$^{-1}$, a quartet of bands at 15 500, 16 300, 17 570 and 20 100 cm$^{-1}$ and doublets at 19 000 and 21 700 cm$^{-1}$, and of low intensity at 25 000 and 26 600 cm$^{-1}$ correspond to the $\alpha$-, $\beta$-, $\gamma$- and $\varepsilon$-type bare Co(II) ions in Al-rich Co-BEA* zeolites. The Vis d–d spectral components of Co-BEA/4.2 in the 13 000–27 000 cm$^{-1}$ range (Fig. 3) also match well those obtained for Al-rich Co-BEA/4.5 and Co-BEA/5.1 samples synthesized and reported in Ref. [42].

The first three spectral components belong to the bare Co(II) ions coordinated with 6MRs of the cationic sites containing AlSiSiAl sequences in the $\alpha$, $\beta$ and $\gamma$ sites (for the framework respective rings see Fig. 1 in Ref. [42], and the latter low intensity doublet reflects bare Co(II) ions balancing a low number of AlSiAl sequences with Al atoms facing the same channel). The d–d spectrum of Co-BEA/11 possessed an identical quartet of frequencies for Co(II)-$\beta$ ions to Al-rich Co-BEA* zeolites, a band at 14 600 cm$^{-1}$ (Co(II)-$\alpha$), a doublet of Co(II)-$\gamma$ ions at 18 500 and 21 700 cm$^{-1}$, and a low-intensity doublet of Co(II)-$\varepsilon$ ions around 25 000 cm$^{-1}$ (cf. Ref. [42]). Among all these bare Co(II) ions, those of the Co(II)-$\beta$ types prevailed (roughly 70–80% of bare Co(II) ions). From the concentration of Co(II)-$\beta$ ions (Table 2), determined from the IR spectra of adsorbed $CD_3CN$ and relative integral intensities of the d–d bands corresponding to the Co(II)-$\alpha$, Co(II)-$\beta$, Co(II)-$\gamma$ and Co(II)-$\varepsilon$ ions, the total concentration of bare Co(II) ions was estimated to equal ~40% of Co content for both Co-BEA/4.2 and Co/BEA/11. As the $[Co(II)(H_2O)_6]^{2+}$ ion-exchange capacity of both the Co-BEA* samples ($c_{Co}$ in Table 2) equals Co/Al ~ 0.5, each $[Co(II)(H_2O)_6]^{2+}$ complex exchanged in hydrated zeolites is attached to two $AlO_4^-$, and thus single far-distant Al atoms are not present. The concentration of Co-oxo species is calculated as the difference between the total Co content ($c_{Co}$) and concentration of bare Co(II) ions ($c_{Co(II)}$) attached to AlSiSiAl in 6MRs in dehydrated Co-BEA* according to Eq. (2).

$$c_{\text{Co-oxo}} = c_{\text{Co}} - c_{\text{Co(II)}} \tag{2}$$

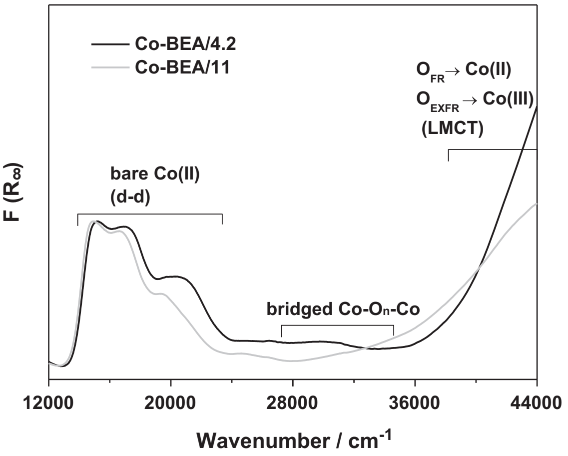

**Fig. 3.** Normalised UV–Vis–NIR spectra of Co-BEA/4.2 and Co-BEA/11 after evacuation at 500 °C for 3 h.

As the Co-oxo species clearly indicated by the $H_2$-TPR experiment (see Fig. 5) cannot be assigned to the $\mu$-oxo dinuclear Co species, because of their negligible concentration in Co-BEA/4.2 and /11 (see UV–Vis spectra in Fig. 3), the structure of the Co-oxo species in dehydrated Co-BEA* (as suggested in the preceding paper [42]) could be represented by a formally trivalent Co ion in a monovalent $[Co(III)O]^+$ complex balancing the charge of one $AlO_4^-$ of unpaired Al atoms located in different rings of the same channel and close enough for binding a cobalt hexaquo complex in hydrated Co-BEA* (see Fig. 4). The second $AlO_4^-$ of unpaired Al atoms binds a proton, which is reflected in the IR spectra of $\nu$ (OH) mode of the dehydrated Co-BEA* (Fig. 2A).

### 3.2.3. Temperature-programmed reduction of Co-BEA* by hydrogen

Fig. 5 compares $H_2$-TPR profiles of Co-BEA/4.2 and /11 pretreated in a stream of air at 450 °C. Co-BEA/11 exhibited hydrogen consumption starting from 650 °C with a maximum at about 840 °C, while the reduction of Co-BEA/4.2 showed more than twice the hydrogen consumption (Table 2) shifted to lower temperature with not pronounced maxima at ca 740, 790 and 840 °C. We have previously shown that the bare Co(II) ions coordinated only with oxygen atoms of 6MRs of the cationic sites containing AlSiSiAl sequences in Si-rich Co-BEA* zeolites are highly stabilized and they are neither oxidized in air at 450 °C nor reduced by hydrogen up to ca 900 °C [42]. Their reduction occurs above 950 °C when partial collapse of the zeolite structure takes place. The absence of the reduction of the bare Co(II) ions in Co-BEA* is in agreement with the well-documented irreducibility of the exchanged Co(II) ions in ZSM-5 [54] and faujasites [55]. Under similar conditions of the $H_2$-TPR experiment bulk cobalt oxide species and oligomeric oxide-like species interacting with the zeolite surface are reduced at temperatures of 250–350 °C and 400 °C, respectively [56,57]. Martínez-Hernández et al. [58,59] attributed hydrogen consumption at 100–350 °C and 350–600 °C in Co-ZSM-5 to the reduction of dispersed $Co_3O_4$ crystallites outside the zeolite pores and dinuclear oxo-cations $[Co—O—Co]^{2+}$ stabilized inside the channels, respectively.

All these findings imply that the temperature range of hydrogen consumption of Co-BEA/4.2 and /11 at 600–900 °C (Fig. 5) reflects reduction of counter Co-oxo ions much more stabilized by negative framework charge compared to supported Co oxides or non-defined oligomeric Co-oxo species. The reduction of Co-BEA* in the 600–900 °C range is also not connected with the $\mu$-oxo dinuclear or oligonuclear Co complexes as these are present only in a negligible concentration (see UV–Vis spectra in Fig. 3).

The consumption of 1.5 mol $H_2$ per mol of a counter Co-oxo ion (Table 2) indicates reduction of formally trivalent Co ions to $Co^0$ with formation of one framework OH group (proton) balancing the resting $AlO_4^-$. At the hydrogen consumption of 1.5 mmol $H_2$ per Co-oxo the concentrations of Co-oxo species in Co-BEA/4.2 and /11 are 0.91 and 0.38 mmol g$^{-1}$. These values are in a good agreement with those calculated as a difference of total Co

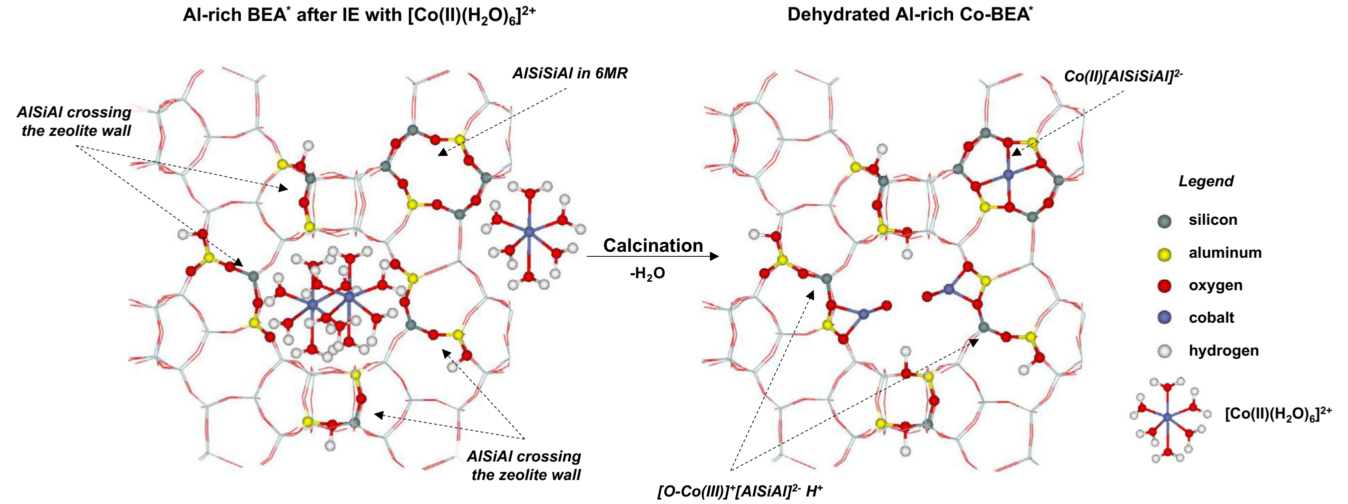

**Fig. 4.** Illustration of the structure of Al-rich BEA* zeolite after ion-exchange with $[Co(II)(H_2O)_6]^{2+}$ and calcination. Hydrated Al-rich Co-BEA* zeolite is binding hexaquo Co(II) complexes by the charge of the framework originating mainly from AlSiAl sequences with Al atoms facing different channels and from AlSiSiAl sequences located in one 6MR-ring ($Al_{pairs}$). After dehydration, bare Co(II) cations compensate charge of AlSiSiAl located in one ring ($Al_{pairs}$) whereas $[Co(III)—O]^+$ and $H^+$ compensate the charge from AlSiAl sequences crossing the zeolite wall and thus facing different channels.

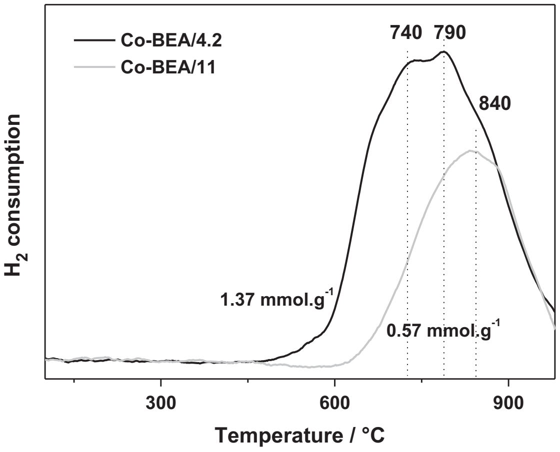

**Fig. 5.** $H_2$-TPR profiles of Co-BEA/4.2 and Co-BEA/11 pre-treated in a stream of air at 450 °C.

concentration and that of bare Co(II) ions according to Eq. (2). The higher hydrogen consumption (ca 2.4 times) and its shift to lower temperatures in Al-rich Co-BEA/4.2 compared to Co-BEA/11 correspond to higher concentration of Co, and indicate their easier reducibility. The easier reducibility of Co-oxo species in Co-BEA/4.2 could stem from their higher density inducing some synergetic effect.

It can be summarized that although the Al-rich BEA/4.2 exhibits a large portion of the framework Al atoms in the AlSiAl sequences (75–100% varying in dependence on their mutual arrangement in the framework, see Ref. [42]) compared to their absence in Si-rich BEA/11 (cf. $^{29}$Si MAS NMR in Fig. 1D), these sequences do not represent sites for binding bare Co(II) ions, as they cross the zeolite wall and their Al atoms face different channels (Fig. 4). The detail analysis of the location of framework Al atoms in Al-rich BEA* given in the preceding paper [42] showed in fact similar distribution of Al atoms in the channels like in Si-rich BEA*, i.e. AlSiSiAl in 6MRs and unpaired Al atoms located in different rings. The bare Co(II) ions are mostly (95%) coordinated with 6MRs containing AlSiSiAl sequences and their relative concentration (ca 40% of the total Co content) attains comparable value like that in Si-rich Co-BEA* (see Table 2). These bare Co(II) ions behave as strong electron-acceptor Lewis sites (Fig. 2B), and they are difficult to reduce by hydrogen, only at very high temperatures (>950 °C) far above those relevant for the SCR-$NO_x$ reaction. The predominated Co-oxo species (ca 60%) are formally trivalent Co ions in a monovalent $[Co(III)O]^+$ entities reflected in strong LMCT absorption ranging from 40000 far above 50000 $cm^{-1}$. The observed easier reduction of counter-ion $[Co(III)O]^+$ species by hydrogen in Al-rich Co-BEA/4.2 compared to those present in Si-rich Co-BEA-11 is attributed to their substantially higher density causing likely some synergetic effect. These Co-oxo species originate from the ion-exchange of $Co(II)(H_2O)_6^{2+}$ complexes in the vicinity of unpaired Al atoms located in different rings, but both facing one channel (Fig. 4). After Co-BEA* dehydration and dehydroxylation, such charge-balancing $[Co(II)(H_2O)_6]^{2+}$ complexes turn out to $[Co(III)O]^+$ species balancing the charge of one $AlO_4^-$ from the unpaired Al atoms, the second one being balanced by a proton. The arrangement of unpaired Al atoms in the channel surface of Al-rich BEA* able to exchange a divalent hexaquo complex originates mostly from the high population of AlSiAl sequences with $AlO_4^-$ located in one ring, but into different channels; for more details see [42].

It should to be pointed out that the template-free Al-rich BEA* samples synthesized and reported here and in Ref. [42], regardless of some differences in conditions of their hydrothermal synthesis, exhibit similar population of bare Co(II) ions (ranging from 30% to 40% of total Co), absence or negligible concentration of the bridged $\mu$-oxo Co(II) complexes, and the rest of the cobalt (60–70% of total Co) represents the counter Co-oxo ions, $[Co(III)O]^+$ (for illustration of binding of bare Co(II) ions and Co-oxo species see Fig. 4).

### 3.3. $C_3H_8$–SCR-$NO_x$

Conversions of $NO_x$ and $C_3H_8$, and CO, $CO_2$ and $N_2O$ yields in the $C_3H_8$–SCR-$NO_x$ reaction in the presence of 1 vol.% water vapor as a function of temperature for Al-rich and Si-rich Co-BEA* zeolites are compared in Fig. 6A–E. At relatively high GHSV of 90000 $h^{-1}$, the $NO_x$ conversion already started at 250 and 320 °C and reached 90% and 14% at 375 °C for Co-BEA/4.2 and Co-BEA/11, respectively. This reflects a considerably lower light-off temperature by up to 70 °C for Co-BEA/4.2 and remarkably improved conversion of $NO_x$ over the entire temperature range. Conversion of $NO_x$ over Si-rich Co-ZSM-5/15, plotted for comparison, exhibits close conversion values to those of Co-BEA/11. The $NO_x$ conversion as well as

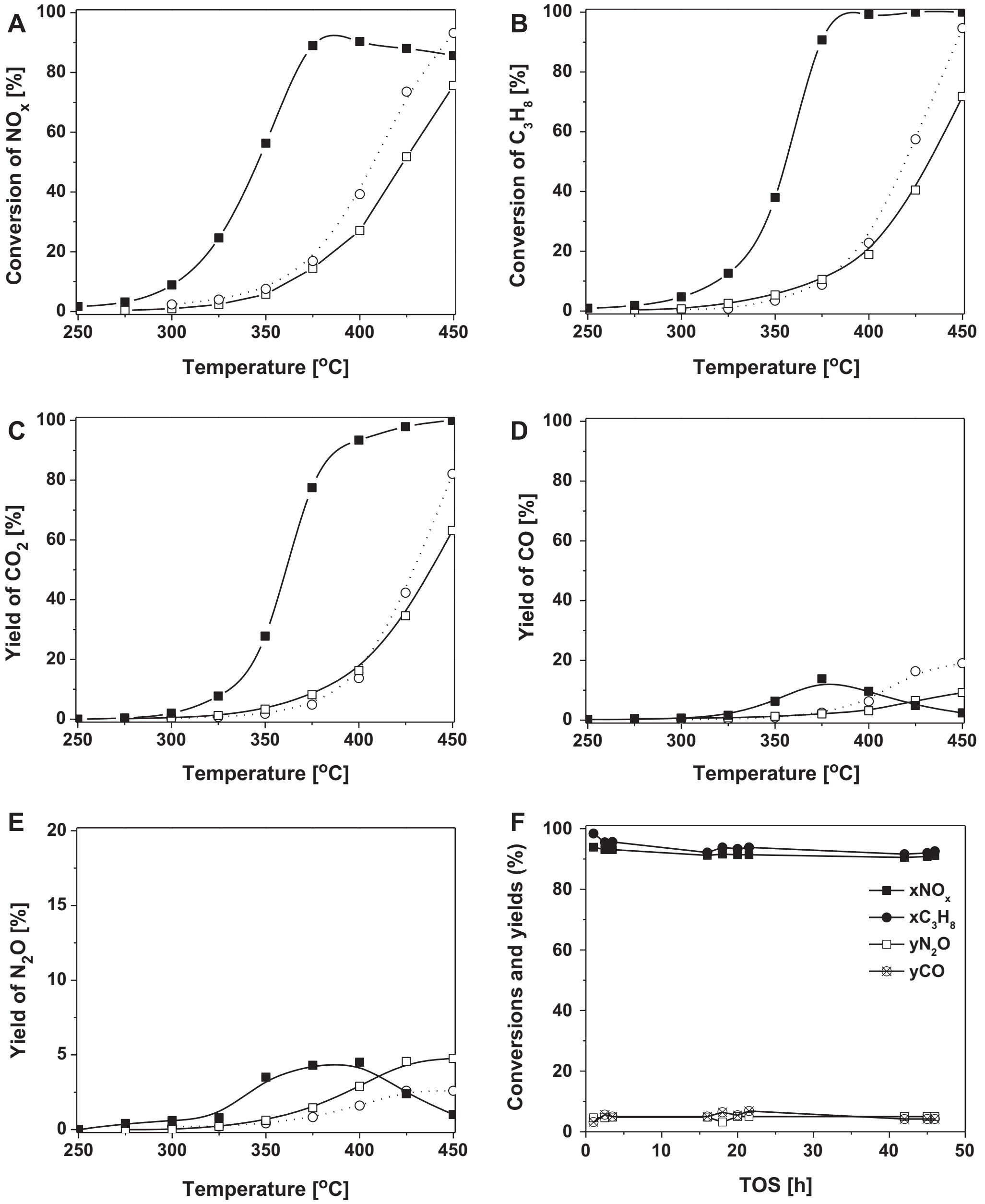

**Fig. 6.** (A)–(E) $C_3H_8$–SCR-NO over Co-BEA/4.2 (■), Co-BEA/11 (□) and Co-ZSM-5/15 (○) catalysts as a function of temperature. Reaction conditions: 1000 ppm NO, 1000 ppm $C_3H_8$, 2.5% $O_2$, and 1% $H_2O$ in He, GHSV 90000 $h^{-1}$. (F) Dependence of conversion of $NO_x$ and $C_3H_8$, and yields of CO and $N_2O$ in $C_3H_8$–SCR-NO on time-on-stream over Co-BEA/4.2. Reaction conditions: 990 ppm NO, 1020 ppm $C_3H_8$, 2.5% $O_2$, and 1% $H_2O$ in He at 375 °C and GHSV 90000 $h^{-1}$.

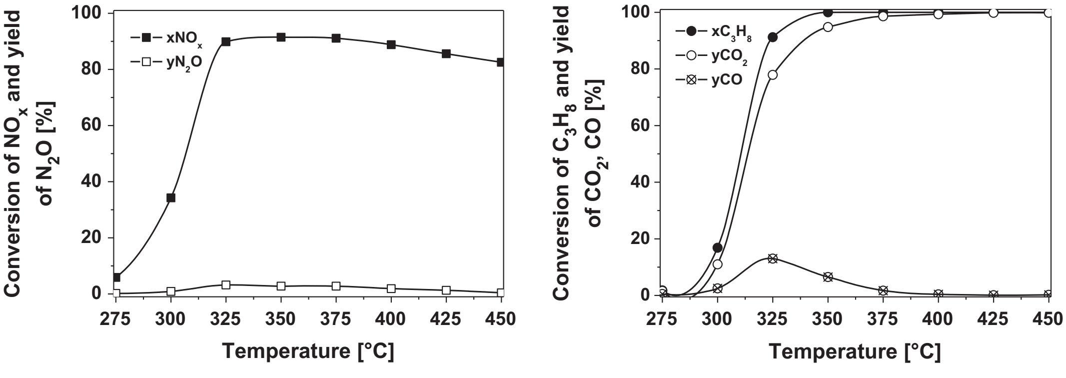

**Fig. 7.** $C_3H_8$–SCR-NO over Co-BEA/4.2 as a function of temperature at a common contact time for stationary deNOx units. Reaction conditions: 1000 ppm NO, 1000 ppm $C_3H_8$, 2.5% $O_2$, and 1% $H_2O$ in He, GHSV 14000 $h^{-1}$.

**Table 3**
Conversion, reaction rates ($r_{SCR}$) and turnover frequencies (TOF) for $C_3H_8$–SCR-$NO_x$. Reaction conditions: 1000 ppm NO, 1000 ppm $C_3H_8$, 2.5% $O_2$ and 1% $H_2O$ in He, GHSV 90 000 $h^{-1}$.

| Sample | Conversion of $NO_x$ (%) | | $r_{SCR}$[a] ($mol_{NO}\ g_{cat}^{-1}\ s^{-1}\ 10^7$) | | $TOF_{Co}$[b] ($mol_{NO}\ mol_{Co}^{-1}\ s^{-1}\ 10^4$) | | $TOF_{Co\text{-}oxo}$[c] ($mol_{NO}\ mol_{Co\text{-}oxo}^{-1}\ s^{-1}\ 10^4$) | | $E_a$[d] (kJ $mol^{-1}$) | lnA[e] |
|---|---|---|---|---|---|---|---|---|---|---|
| | 325 °C | 350 °C | 325 °C | 350 °C | 325 °C | 350 °C | 325 °C | 350 °C | | |
| Co-BEA/4.2 | 24.6 | 56.3 | 6.4 | 17.7 | 4.3 | 12.7 | 7.4 | 22.0 | 123.4 | 13.7 |
| Co-BEA/11 | 2.4 | 5.8 | 0.55 | 1.4 | 0.8 | 2.0 | 1.4 | 3.5 | 116.3 | 9.7 |

[a] Rates calculated using the first-order kinetics.
[b] TOF calculated for total concentration of cobalt.
[c] TOF calculated for Co-oxo species.
[d] Apparent activation energy.
[e] The pre-exponential factor.

propane conversion and $N_2O$ and CO yields were very stable in time-on-stream for 45 h at 375 °C (Fig. 6F). Conversion of propane as a function of temperature follows the trend of $NO_x$ conversion on both Co-BEA*, similarly as the yield of $CO_2$. This indicates effective use of propane as a reductant of $NO_x$ to nitrogen in the whole temperature range. The yields of $N_2O$ over Co-BEA/4.2 are low (∼2%) and only under conditions of high propane conversion (close to 100%) reach 4% at 93% $NO_x$ conversion at 400 °C. A higher selectivity for $N_2O$ was obtained over Co-BEA/11. The yields of CO did not exceed 15%. If $C_3H_8$–SCR-$NO_x$ over Co-BEA/4.2 was carried out under conditions similar to real gas streams, i.e. at GHSV 14 000 $h^{-1}$ and 1 vol.% $H_2O$ (Fig. 7), high $NO_x$ conversion and similar selectivity were obtained at much lower temperatures with $NO_x$ conversion onset at 270 °C and reaching 90% $NO_x$ conversion at 325 °C.

It is known that the high excess of water in $NO_x$ streams used in our kinetic experiments (10 000–100 000 ppm $H_2O$ vs. 1000 ppm NO) representing real wet $NO_x$ streams greatly suppresses the activity of bare Co ions in zeolites, specifically in the temperature range below 400 °C, when water molecules are strongly adsorbed on these Co ions with Lewis character [21,22]. Therefore, in the wet $NO_x$ feed the $[Co(III)O]^+$ oxo-species can be supposed to be the only or the most active sites. The extra-framework oxygen ligated to the Co ion preserves it against water adsorption like it restricts $d_3$-acetonitrile [21,22].

The reaction rates of $NO_x$ conversion and turn-over-frequency values per total Co ($TOF_{Co}$) and Co-oxo species ($TOF_{Co\text{-}oxo}$) for Co-BEA* zeolites are given in Table 3. The reaction rates at 325 and 350 °C for Al-rich Co-BEA/4.2 are twelve times higher, and $TOF_{Co}$ and $TOF_{Co\text{-}oxo}$ are five-to-six times higher than those over Co-BEA/11. The Arrhenius plots of the logarithm of the reaction rate vs. reciprocal temperature (Fig. 8) yield linear dependences of different intercept axes for Al-rich and Si-rich Co-BEA*. The apparent activation energies ($E_a$) are close, around 120 kJ $mol^{-1}$, for Al-rich and Si-rich Co-BEA*, indicating a similar reaction mechanism. But a substantially higher pre-exponential factor A for Co-BEA/4.2 reflecting high concentration and density of Co species compensates $E_a$ to match the higher reaction rates. The twelve times higher reaction rates per gram of a zeolite and five to six times higher TOF per Co and per Co-oxo species in Al-rich Co-BEA/4.2, while the concentration of Co is only 2.1 times higher and the relative population of counter-ion Co-oxo species is similar, indicate the presence of Co-oxo species, which greatly outperform those in

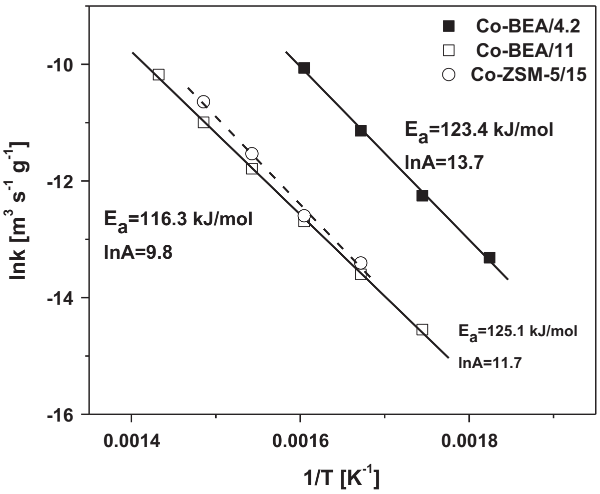

**Fig. 8.** Arrhenius plot with the pre-exponential factors ln*A* and apparent activation energies for Co-BEA/4.2 (■), Co-BEA/11 (□) and Co-ZSM-5/15 (○) catalysts. Reaction conditions as in Fig. 6A.

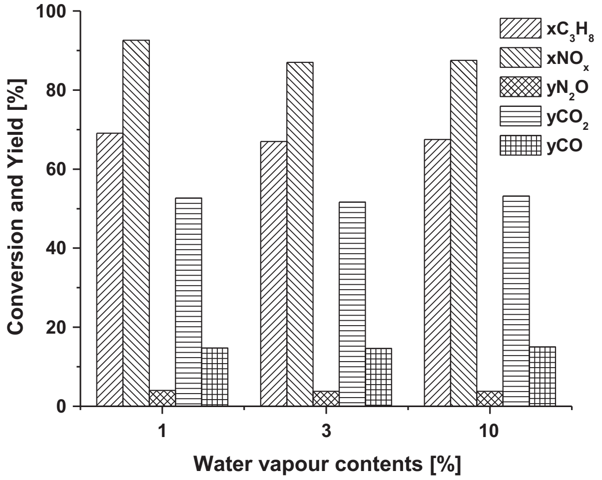

**Fig. 9.** Effect of water vapor in the feed on $C_3H_8$–SCR-NO activity over Co-BEA/4.2. Reaction conditions: 1000 ppm NO, 1000 ppm $C_3H_8$, 2.5% $O_2$, and 1–10% $H_2O$ in He, T 400 °C, GHSV 90000 $h^{-1}$.

Co-BEA/11. The higher activity of Co-oxo species in Co-BEA/4.2 is supported by their easier reducibility as clearly observed in the $H_2$-TPR experiment (Fig. 5). As the bare Co(II)-$\varepsilon$ ions (low concentration) attached to AlSiAl evidently also exhibit Lewis properties, like those in $\alpha$, $\beta$, and $\gamma$ sites, and the dinuclear $[\text{Co—O—Co}]^{2+}$ complexes are of negligible concentration in Co-BEA* we can speculate that the high concentration and density of counter-ion Co-oxo species attained in Al-rich Co-BEA/4.2 (see Fig. 4) result in their synergetic effect manifested both in their reduction by hydrogen and the $C_3H_8$–SCR-$NO_x$ reaction.

The "after-treatment" of $NO_x$ gases coming from the burning processes of diesel engines and gas turbines is typical in the presence of water vapor, which usually dramatically decreases $NO_x$ conversion. With Al-rich Co-BEA/4.2, variation in the concentration of water vapor from 1% to 10% did not significantly affect the $NO_x$ conversion and product composition of the SCR-$NO_x$ reaction at 400 °C and GHSV of 90000 $h^{-1}$ (Fig. 9) as well as at 350 °C (not shown). The high and stable activity of Co-BEA/4.2 in a $NO_x$ stream containing up to 10% water vapor is an additional support for the $[\text{Co(III)O}]^+$ entity being the most active site in SCR-$NO_x$.

To highlight the exceptionally high activity of the Al rich Co-BEA* zeolite Table 4 lists the activities of Co- and Cu-zeolites of various structures and compositions as found in the open literature under comparable conditions of the $C_3H_8$–SCR-$NO_x$ process with attention to the real gas streams compositions [2,7,9,22,60–63]. For comparison the data for 64 samples of metal loaded alumina samples summarized in Ref. [64] are also included. Without any doubt, cobalt and copper zeolites outperform metal oxides supported on alumina. This emphasizes the unique activity of counter-ion Co and Cu species ligated in zeolites. For $C_3H_8$–SCR-$NO_x$, cobalt is the element of the best choice compared to less active copper. The Si-rich zeolites of Si/Al > 12 and pentasil ring structure (MFI, BEA*), and with Co loading to a maximum degree provide comparable activity. The surprisingly low activity of Co-FER might be a result of the narrow pores, unaccessibility of some Co ions as well as distribution of Al atoms in the ferrierite framework. The absence of redox activity for Co ions in faujasites [7] is also well known for other metals, and this is attributed to the high density of Al atoms (negative charge) in the framework and the predominant formation of bare difficult reduced Co ions coordinated with framework oxygen atoms. Even a high content of Co in mordenite (Si/Al 5.5, Co/Al 0.37) did not bring about the activity comparable with Al-rich Co-BEA* (Si/Al 4.2, Co/Al 0.54), albeit the Co content was substantially increased compared to Co-ZSM-5 and Co-BEA of Si/Al ~ 12 or 22. This finding indicates that not only the concentration of Al atoms in the framework controlling the Co ion-exchange capacity, but especially the arrangement of Al atoms controlling the local negative charge of the framework and provid-

**Table 4**
$C_3H_8$–SCR-NO activity of Co-BEA/4.2 and Co- and Cu-zeolites of various topologies and compositions reported in the open literature.

| Catalyst | Conversion of $NO_x$ (%) | | GHSV ($h^{-1}$) | Concentration (ppm) | | | | Reference |
|---|---|---|---|---|---|---|---|---|
| | 300 °C | 400 °C | | NO | $C_3H_8$ | $O_2$ | $H_2O$ | |
| **Co-BEA/4.2** (Si/Al 4.2; Co/Al 0.49; Co 8.7%) | **9** | **90** | **90000** | 1000 | 1000 | 2.5% | 1% | This study |
| | **36** | **90** | **14000** | | | | | |
| | – | **88** | **90000** | 1000 | 1000 | 2.5% | 10% | |
| Co-BEA/11 (Si/Al 11.3, Co/Al 0.54, Co 4.1%) | 1 | 27 | 90000 | 1000 | 1000 | 2.5% | 1% | This study |
| Co-ZSM-5/15 (Si/Al 15, Co/Al 0.42, Co 2.5%) | 2 | 39 | | | | | | |
| Co-BEA (Si/Al 26.5, Co 1.1%) | 10 | 40 | 15000 | 1000 | 1000 | 5% | 10% | [9] |
| Co-BEA (Si/Al 24, Co 1.13%) | 10 | 60 | | | | | | |
| Co-BEA (Si/Al 23.1, Co 1.35%) | 10 | 70 | | | | | | |
| Co-BEA (Si/Al 20.4, Co 1.29%) | 16 | 58 | | | | | | |
| Co-BEA (Si/Al 11.9, Co/Al 0.50) | 0 | 83 | 30000 | 1000 | 1000 | 2.5% | 10% | [22] |
| Co-FAU (Si/Al 2.4, Co/Al 0.32) | 0 | 0 | 15000 | 500 | 1000 | 10% | 9% | [7] |
| Co-FER (Si/Al 10, Co/Al 0.47) | – | 14.9 | | | | | | |
| Co-MOR (Si/Al 5.5, Co/Al 0.37) | 11 | 54.2 | | | | | | |
| Co-ZSM-5 (Si/Al 25, Co/Al 0.55) | 9.1 | 65.6 | | | | | | |
| Co-BEA (Si/Al 11.2, Co/Al 0.4) | 0 | 83.7 | | | | | | |
| Co-BEA (Co/Al 0.49) | – | 78 | 15000 | 150 | 500 | 10% | 9% | [2] |
| Co-ZSM-5 (Co/Al 0.53) | – | 50 | | | | | | |
| Co-BEA (Si/Al 22.5, Co 2.2%) | – | 83.4 | 15000 | 500 | 1000 | 10% | 9% | [60] |
| Co-FER (Si/Al 8, Co 1.29%) | 0.9 | 1.7 | | | | | | |
| Cu-ZSM-5 (Si/Al 13, Cu/Al 0.5) | 2 | 24 | 30000 | 1000 | 1500 | 6% | 12% | [61] |
| Cu-ZSM-5 (Si/Al 25, Cu 2.4%) | 4 | 28 | 30000 | 1000 | 1000 | 5% | 5% | [62] |
| Cu-ZSM-5 (Si/Al 25, Cu/Al 0.53) | 4.3 | 22.5 | 15000 | 500 | 1000 | 10% | 9% | [7] |
| Cu-BEA (Si/Al 11, Cu/Al 0.53) | 1.2 | 20.8 | | | | | | |
| Cu-ZSM-5 (Si/Al 21, IE Cu 90%, Cu 1.03%) | 2 | 19 | 102000 | 645 | 1320 | 1% | 14% | [63] |
| 64 samples of Ag–, Co–, Cu–, In–$Al_2O_3$ | – | 12–38 | 36000 | 1500 | 1500 | 5% | 0% | [64] |

ing sites for binding counter-ion Co-oxo species in high concentrations is a decisive parameter for the $C_3H_8$–SCR-$NO_x$ activity and its stability in the presence of water vapor in the feed.

## 4. Conclusions

The study reports the unparallel high $C_3H_8$–SCR-$NO_x$ activity of the hydrothermally template-free synthesized Al-rich Co-BEA* zeolite (Si/Al 4.2, Co/Al 0.5) preserved even in the presence of water vapor in $NO_x$ streams containing up to 10 vol.%. A dramatic increase in the SCR activity of Al-rich compared to much less active Si-rich Co-BEA* (Si/Al 11 and Co/Al 0.5) (the previously reported as the most active) is documented by twelve times higher reaction rate and five-to-six times higher TOF per total Co or Co-oxo. This extra-ordinarily high and stable activity of Al rich Co-BEA* originates from the increased concentration of Al in the framework, corresponding increased concentration and density of counter-ion Co-oxo species, and as suggested their synergetic effect also reflected in their increased reducibility.

The increased concentration of Al atoms in the framework of Al-rich BEA*, albeit resulting in the high population of AlSiAl sequences (in contrast to their absence in Si-rich BEA*) does not result in relative increased binding of bare non-reducible Co(II) ions attached to AlSiAl sequences. As the AlSiAl sequences are crossing the zeolite beta wall (Fig. 4) they cannot bind the bare Co(II) ions. This in fact results in an increased concentration of similar Si–Al arrangements in the surface of channels like those existing in Si-rich Co-BEA*. This leads to high concentration of similar framework sites for binding counter-ion metal species, i.e. both bare Co(II) ions and Co-oxo species. The bare Co(II) ions coordinated with framework oxygen atoms of 6MRs with AlSiSiAl sequences exhibit strong Lewis, but not redox behavior, and are not SCR active in wet $NO_x$ streams. The most active sites are represented by formally trivalent Co in a monovalent $[Co(III)O]^+$ entities, exhibiting via extra-framework oxygen ligand redox behavior, and not adsorbing bases as water molecules. These $[Co(III)O]^+$ species are charge balanced by the $AlO_4^-$ of unpaired Al atoms located in different rings and facing the same channel (Fig. 4). While $[Co(III)O]^+$ are present in both the Al-rich and Si-rich BEA*, their high density in Al-rich Co-BEA* induces increased reducibility and extra-ordinarily high redox activity in $C_3H_8$–SCR-$NO_x$. An extra-framework oxygen bound to Co ions in $[Co(III)O]^+$ advantageously preserves these most active sites against adsorption of bases as water molecules in $NO_x$ streams up to 10 vol.%.

## Acknowledgments

This study was supported by the Technology Agency of the Czech Republic (Project # TH01021259), the Czech Science Foundation (Project # 15-13876S), and by RVO # 61388955.

## Appendix A. Supplementary material

Supplementary data associated with this article can be found, in the online version, at http://dx.doi.org/10.1016/j.jcat.2015.10.007.

## References

[1] F. Witzel, G.A. Sill, W.K. Hall, Reaction studies of the selective reduction of NO by various hydrocarbons, J. Catal. 149 (1994) 229–237.
[2] Y. Traa, B. Burger, J. Weitkamp, Zeolite-based materials for the selective catalytic reduction of NOx with hydrocarbons, Microporous Mesoporous Mater. 30 (1999) 3–41.
[3] R. Burch, Knowledge and know-how in emission control for mobile applications, Catal. Rev. – Sci. Eng. 46 (2004) 271–333.
[4] Z. Liu, S. Ihl Woo, Recent advances in catalytic DeNOx science and technology, Catal. Rev. – Sci. Eng. 48 (2006) 43–89.
[5] M.V. Twigg, Progress and future challenges in controlling automotive exhaust gas emissions, Appl. Catal. B: Environ. 70 (2007) 2–15.
[6] T. Tabata, M. Kokitsu, H. Ohtsuka, O. Okada, L.M.F. Sabatino, G. Bellussi, Study on catalysts of selective reduction of NOx using hydrocarbons for natural gas engines, Catal. Today 27 (1996) 91–98.
[7] T. Tabata, H. Ohtsuka, L.M.F. Sabatino, G. Bellussi, Selective catalytic reduction of NOx by propane on Co-loaded zeolites, Microporous Mesoporous Mater. 21 (1998) 517–524.
[8] P. Sazama, O. Bortnovsky, J. Dedecek, Z. Tvaruzkova, Z. Sobalik, Geopolymer based catalysts – new group of catalytic materials, Catal. Today 164 (2011) 92–99.
[9] H.H. Chen, S.C. Shen, X. Chen, S. Kawi, Selective catalytic reduction of NO over Co/beta-zeolite: effects of synthesis condition of beta-zeolites, Co precursor, Co loading method and reductant, Appl. Catal. B: Environ. 50 (2004) 37–47.
[10] M.C. Campa, S. De Rossi, G. Ferraris, V. Indovina, Catalytic activity of Co-ZSM-5 for the abatement of NOx with methane in the presence of oxygen, Appl. Catal. B: Environ. 8 (1996) 315–331.
[11] L.B. Gutierrez, E.E. Miro, M.A. Ulla, Effect of the location of cobalt species on NO adsorption and NOx-SCR over Co-mordenite, Appl. Catal. A: Gen. 321 (2007) 7–16.
[12] J. Janas, T. Machej, J. Gurgul, R.P. Socha, M. Che, S. Dzwigaj, Effect of Co content on the catalytic activity of CoSiBEA zeolite in the selective catalytic reduction of NO with ethanol: nature of the cobalt species, Appl. Catal. B: Environ. 75 (2007) 239–248.
[13] A.E. Palomares, C. Franch, A. Corma, Determining the characteristics of a Co-zeolite to be active for the selective catalytic reduction of NOx with hydrocarbons, Catal. Today 176 (2011) 239–241.
[14] J.H. Park, C.H. Park, I.S. Nam, Characteristics of wet and solid ion exchanged Co-ferrierite catalysts for the reduction of NO using methane, Appl. Catal. A: Gen. 277 (2004) 271–279.
[15] P. Pietrzyk, C. Dujardin, K. Gora-Marek, P. Granger, Z. Sojka, Spectroscopic IR, EPR, and operando DRIFT insights into surface reaction pathways of selective reduction of NO by propene over the Co-BEA zeolite, Phys. Chem. Chem. Phys. 14 (2012) 2203–2215.
[16] P. Pietrzyk, Z. Sojka, $Co^{2+}/Co^0$ redox couple revealed by EPR spectroscopy triggers preferential coordination of reactants during SCR of NOx with propene over cobalt-exchanged zeolites, Chem. Commun. (2007) 1930–1932.
[17] C. Resini, T. Montanari, L. Nappi, G. Bagnasco, M. Turco, G. Busca, F. Bregani, M. Notaro, G. Rocchini, Selective catalytic reduction of NOx by methane over Co-H-MFI and Co-H-FER zeolite catalysts: characterisation and catalytic activity, J. Catal. 214 (2003) 179–190.
[18] A. De Lucas, J.L. Valverde, F. Dorado, A. Romero, I. Asencio, Influence of the ion exchanged metal (Cu Co, Ni and Mn) on the selective catalytic reduction of NOx over mordenite and ZSM-5, J. Mol. Catal. A: Chem. 225 (2005) 47–58.
[19] J. Dedecek, L. Capek, P. Sazama, Z. Sobalik, B. Wichterlova, Control of metal ion species in zeolites by distribution of aluminium in the framework: from structural analysis to performance under real conditions of SCR-NOx and NO, $N_2O$ decomposition, Appl. Catal. A: Gen. 391 (2011) 244–253.
[20] Z. Sobalik, P. Sazama, J. Dedecek, B. Wichterlova, Critical evaluation of the role of the distribution of Al atoms in the framework for the activity of metallo-zeolites in redox $N_2O$/NOx reactions, Appl. Catal. A: Gen. 474 (2014) 178–185.
[21] L. Capek, J. Dedecek, P. Sazama, B. Wichterlova, The decisive role of the distribution of Al in the framework of beta zeolites on the structure and activity of Co ion species in propane–SCR-NOx in the presence of water vapour, J. Catal. 272 (2010) 44–54.
[22] L. Capek, J. Dedecek, B. Wichterlova, Co-beta zeolite highly active in propane–SCR-NOx in the presence of water vapor: effect of zeolite preparation and A1 distribution in the framework, J. Catal. 227 (2004) 352–366.
[23] R.B. Borade, A. Clearfield, Preparation of aluminum-rich Beta zeolite, Microporous Mater. 5 (1996) 289–297.
[24] R.B. Borade, A. Clearfield, Synthesis of beta zeolite with high levels of tetrahedral aluminium, Chem. Commun. (1996) 625–626.
[25] B. Xie, J. Song, L. Ren, Y. Ji, J. Li, F.S. Xiao, Organotemplate-free and fast route for synthesizing beta zeolite, Chem. Mater. 20 (2008) 4533–4535.
[26] K. Shanjiao, D. Tao, L. Qiang, D. Aijun, Z. Yanying, P. Huifang, Preparation and application of zeolite beta with super-low $SiO_2/Al_2O_3$ ratio, J. Porous Mater. 15 (2008) 159–162.
[27] G. Majano, L. Delmotte, V. Valtchev, S. Mintova, Al-rich zeolite beta by seeding in the absence of organic template, Chem. Mater. 21 (2009) 4184–4191.
[28] Y. Kamimura, W. Chaikittisilp, K. Itabashi, A. Shimojima, T. Okubo, Critical factors in the seed-assisted synthesis of zeolite beta and "green beta" from OSDA-free $Na^+$-aluminosilicate gels, Chem. – Asian J. 5 (2010) 2182–2191.
[29] Y. Kamimura, S. Tanahashi, K. Itabashi, A. Sugawara, T. Wakihara, A. Shimojima, T. Okubo, Crystallization behavior of zeolite beta in OSDA-free, seed-assisted synthesis, J. Phys. Chem. C 115 (2011) 744–750.
[30] B. Xie, H. Zhang, C. Yang, S. Liu, L. Ren, L. Zhang, X. Meng, B. Yilmaz, U. Muller, F.-S. Xiao, Seed-directed synthesis of zeolites with enhanced performance in the absence of organic templates, Chem. Commun. 47 (2011) 3945–3947.
[31] K. Itabashi, Y. Kamimura, K. Iyoki, A. Shimojima, T. Okubo, A working hypothesis for broadening framework types of zeolites in seed-assisted synthesis without organic structure-directing agent, J. Am. Chem. Soc. 134 (2012) 11542–11549.
[32] B. Yilmaz, U. Muller, M. Feyen, S. Maurer, H. Zhang, X. Meng, F.S. Xiao, X. Bao, W. Zhang, H. Imai, T. Yokoi, T. Tatsumi, H. Gies, T. De Baerdemaeker, D. De Vos, A new catalyst platform: zeolite Beta from template-free synthesis, Catal. Sci. Technol. 3 (2013) 2580–2586.

[33] T. De Baerdemaeker, B. Yilmaz, U. Muller, M. Feyen, F.S. Xiao, W. Zhang, T. Tatsumi, H. Gies, X. Bao, D. De Vos, Catalytic applications of OSDA-free Beta zeolite, J. Catal. 308 (2013) 73–81.

[34] H. Zhang, B. Xie, X. Meng, U. Mueller, B. Yilmaz, M. Feyen, S. Maurer, H. Gies, T. Tatsumi, X. Bao, W. Zhang, D. De Vos, F.-S. Xiao, Rational synthesis of Beta zeolite with improved quality by decreasing crystallization temperature in organotemplate-free route, Microporous Mesoporous Mater. 180 (2013) 123–129.

[35] Y. Kubota, K. Itabashi, S. Inagaki, Y. Nishita, R. Komatsu, Y. Tsuboi, S. Shinoda, T. Okubo, Effective fabrication of catalysts from large-pore, multidimensional zeolites synthesized without using organic structure-directing agents, Chem. Mater. 26 (2014) 1250–1259.

[36] B. Zheng, Y. Wan, W. Yang, F. Ling, H. Xie, X. Fang, H. Guo, Mechanism of seeding in hydrothermal synthesis of zeolite Beta with organic structure-directing agent-free gel, Chin. J. Catal. 35 (2014) 1800–1810.

[37] P. Sazama, B. Wichterlova, S. Sklenak, V.I. Parvulescu, N. Candu, G. Sadovska, J. Dedecek, P. Klein, V. Pashkova, P. Stastny, Acid and redox activity of template-free Al-rich H-BEA* and Fe-BEA* zeolites, J. Catal. 318 (2014) 22–33.

[38] H. Zhang, L. Chu, Q. Xiao, L. Zhu, C. Yang, X. Meng, F.-S. Xiao, One-pot synthesis of Fe-Beta zeolite by an organotemplate-free and seed-directed route, J. Mater. Chem. A 1 (2013) 3254–3257.

[39] L. Xu, C. Shi, Z. Zhang, H. Gies, F.-S. Xiao, D. De Vos, T. Yokoi, X. Bao, M. Feyen, S. Maurer, B. Yilmaz, U. Mueller, W. Zhang, Enhancement of low-temperature activity over Cu-exchanged zeolite beta from organotemplate-free synthesis for the selective catalytic reduction of NO with $NH_3$ in exhaust gas streams, Microporous Mesoporous Mater. 200 (2014) 304–310.

[40] C.Y. Chen, Q.M. Wu, F. Chen, L. Zhang, S.X. Pan, C.Q. Bian, X.M. Zheng, X.J. Meng, F.S. Xiao, Aluminium-rich Beta zeolite-supported platinum nanoparticles for the low-temperature catalytic removal of toluene, J. Mater. Chem. A 3 (2015) 5556–5562.

[41] M. Ogura, K. Itabashi, J. Dedecek, T. Onkawa, Y. Shimada, K. Kawakami, K. Onodera, S. Nakamura, T. Okubo, Stabilization of bare divalent Fe(II) cations in Al-rich beta zeolites for superior NO adsorption, J. Catal. 315 (2014) 1–5.

[42] P. Sazama, E. Tabor, P. Klein, B. Wichterlova, S. Sklenak, L. Mokrzycki, V. Pashkkova, M. Ogura, J. Dedecek, Al-rich beta zeolites. Distribution of Al atoms in the framework and related protonic and metal-ion species, J. Catal. (2015) accepted for publication, http://dx.doi.org/10.1016/.jcat.2015.10.010.

[43] P. Sazama, B. Wichterlova, E. Tabor, P. Stastny, N.K. Sathu, Z. Sobalik, J. Dedecek, S. Sklenak, P. Klein, A. Vondrova, Tailoring of the structure of Fe-cationic species in Fe-ZSM-5 by distribution of Al atoms in the framework for $N_2O$ decomposition and $NH_3$–SCR-NOx, J. Catal. 312 (2014) 123–138.

[44] C.A. Fyfe, Y. Feng, H. Grondey, G.T. Kokotailo, H. Gies, One- and two-dimensional high-resolution solid-state NMR studies of zeolite lattice structures, Chem. Rev. 91 (1991) 1525–1543.

[45] S. Civis, D. Babankova, J. Cihelka, P. Sazama, L. Juha, Spectroscopic investigations of high-power laser-induced dielectric breakdown in gas mixtures containing carbon monoxide, J. Phys. Chem. A 112 (2008) 7162–7169.

[46] A. Shichi, A. Satsuma, T. Hattori, Influence of hydrocarbon molecular size on the selective catalytic reduction of NO by hydrocarbons over Cu-MFI zeolite, Appl. Catal. A: Gen. 207 (2001) 315–321.

[47] P. Sazama, N.K. Sathu, E. Tabor, B. Wichterlova, S. Sklenak, Z. Sobalik, Structure and critical function of Fe and acid sites in Fe-ZSM-5 in propane oxidative dehydrogenation with $N_2O$ and $N_2O$ decomposition, J. Catal. 299 (2013) 188–203.

[48] M.M.J. Treacy, J.M. Newsam, Two new three-dimensional twelve-ring zeolite frameworks of which zeolite beta is a disordered intergrowth, Nature 332 (1988) 249–251.

[49] R.W. Joyner, A.D. Smith, M. Stockenhuber, M.W.E. Van Den Berg, The local structure of aluminium sites in zeolites, Phys. Chem. Chem. Phys. 6 (2004) 5435–5439.

[50] B.H. Wouters, T. Chen, P.J. Grobet, Steaming of zeolite Y: formation of transient Al species, J. Phys. Chem. B 105 (2001) 1135–1139.

[51] P. Sazama, B. Wichterlova, J. Dedecek, Z. Tvaruzkova, Z. Musilova, L. Palumbo, S. Sklenak, O. Gonsiorova, FTIR and 27Al MAS NMR analysis of the effect of framework Al- and Si-defects in micro- and micro-mesoporous H-ZSM-5 on conversion of methanol to hydrocarbons, Microporous Mesoporous Mater. 143 (2011) 87–96.

[52] C. Paze, A. Zecchina, S. Spera, A. Cosma, E. Merlo, G. Spano, G. Girotti, Comparative IR and $^1H$ MAS NMR study of adsorption of $CD_3CN$ on zeolite H-beta: evidence of the presence of two families of bridged Bronsted sites, Phys. Chem. Chem. Phys. 1 (1999) 2627–2629.

[53] J. Dedecek, L. Capek, D. Kaucky, Z. Sobalik, B. Wichterlova, Siting and distribution of the Co ions in beta zeolite: a UV–Vis–NIR and FTIR study, J. Catal. 211 (2002) 198–207.

[54] X.Y. Chen, S.C. Shen, H.H. Chen, S. Kawi, SCR of lean NOx with $C_3H_8$ over Co/MFI catalysts: dependence on synthesis condition of MFI and Co location, J. Catal. 221 (2004) 137–147.

[55] Q. Tang, Q. Zhang, P. Wang, Y. Wang, H. Wan, Characterizations of cobalt oxide nanoparticles within faujasite zeolites and the formation of metallic cobalt, Chem. Mater. 16 (2004) 1967–1976.

[56] R.S. da Cruz, A.J.S. Mascarenhas, H.M.C. Andrade, Co-ZSM-5 catalysts for $N_2O$ decomposition, Appl. Catal. B: Environ. 18 (1998) 223–231.

[57] M. Suzuki, K. Tsutsumi, H. Takahashi, Y. Saito, T.p.r. study on hydrolysis character of $Co^{2+}$ ions in Y zeolite, Zeolites 8 (1988) 381–386.

[58] A. Martínez-Hernández, G.A. Fuentes, Redistribution of cobalt species in Co-ZSM-5 during operation under wet conditions in the reduction of NOx by propane, Appl. Catal. B: Environ. 57 (2005) 167–174.

[59] A. Martínez-Hernández, G.A. Fuentes, S.A. Gómez, Selective catalytic reduction of NOx with $C_3H_8$ using Co-ZSM-5 and Co-MOR as catalysts: a model to account for the irreversible deactivation promoted by $H_2O$, Appl. Catal. B: Environ. 166–167 (2015) 465–474.

[60] O. Okada, T. Tabata, M. Kokitsu, H. Ohtsuka, L.M.F. Sabatino, G. Bellussi, Advanced catalyst for NOx reduction using hydrocarbons from lean-burning gas engine, Appl. Surf. Sci. 121 (1997) 267–272.

[61] L. Capek, K. Novoveska, Z. Sobalik, B. Wichterlova, L. Cider, E. Jobson, Cu-ZSM-5 zeolite highly active in reduction of NO with decane under water vapor presence: comparison of decane, propane and propene by in situ FTIR, Appl. Catal. B: Environ. 60 (2005) 201–210.

[62] L. Li, N. Guan, HC-SCR reaction pathways on ion exchanged ZSM-5 catalysts, Microporous Mesoporous Mater. 117 (2009) 450–457.

[63] R. Gopalakrishnan, P.R. Stafford, J.E. Davidson, W.C. Hecker, C.H. Bartholomew, Selective catalytic reduction of nitric oxide by propane in oxidizing atmosphere over copper-exchanged zeolites, Appl. Catal. B: Environ. 2 (1993) 165–182.

[64] M. Richter, M. Langpape, S. Kolf, G. Grubert, R. Eckelt, J. Radnik, M. Schneider, M.M. Pohl, R. Fricke, Combinatorial preparation and high-throughput catalytic tests of multi-component deNOx catalysts, Appl. Catal. B: Environ. 36 (2002) 261–277.